


## PAPER

[View Article Online](#)  
[View Journal](#) | [View Issue](#)
Cite this: *Nanoscale*, 2022, **14**, 15691

# Co-doping of tellurium with bismuth enhances stability and photoluminescence quantum yield of Cs<sub>2</sub>AgInCl<sub>6</sub> double perovskite nanocrystals†

 Shixun Wang,<sup>‡a</sup> Ran Shi,<sup>‡b</sup> Bing Tang,<sup>a</sup> Yuan Xiong,<sup>a</sup> Arsenii Portniagin,<sup>a</sup> Xin Zhao,<sup>a</sup> Stephen V. Kershaw,<sup>a</sup> Run Long <sup>\*b</sup> and Andrey L. Rogach <sup>\*a</sup>

The co-doping of double perovskites is a useful approach in terms of improving their stability and photoluminescence quantum yield. Herein, Bi<sup>3+</sup> and Te<sup>4+</sup> cations have been co-doped into Cs<sub>2</sub>AgInCl<sub>6</sub> nanocrystals. Doping with Te<sup>4+</sup> cations promotes radiative recombination of self-trapped excitons due to increased defect formation energies of silver and indium vacancies, according to experimental and theoretical results. When used in excess, the TeO<sub>2</sub> precursor would generate residual TeO<sub>2</sub>, Te<sub>2</sub>O<sub>3</sub>Cl<sub>2</sub>, R<sub>2</sub>TeO, or all three of them, which confined undesired chlorine ions on oxygen vacancies to counteract the pull from the Cs<sub>2</sub>AgInCl<sub>6</sub> host, resulting in improved coordination with surface oleic acid ligands. As a result, 1% Bi and 8% Te co-doped Cs<sub>2</sub>AgInCl<sub>6</sub> nanocrystals reach a high photoluminescence quantum yield of 34% and show an improved stability, maintaining over 70% of their original emission intensity after storage for more than 1 month. These findings are important in the context of producing high-performance properly doped double perovskite nanocrystals for optoelectronic applications.

 Received 29th August 2022,  
 Accepted 13th October 2022

DOI: 10.1039/d2nr04717a

[rsc.li/nanoscale](https://rsc.li/nanoscale)

## Introduction

Owing to their useful optoelectronic properties such as high charge-carrier mobility, tunable bandgap, high photoluminescence quantum yield (PL QY), and facile solution synthesis, all-inorganic lead halide perovskite (CsPbX<sub>3</sub>, X = Cl, Br, I) nanocrystals (NCs) have attracted immense attention in the past several years.<sup>1–4</sup> Severe concerns still remain due to both the presence of toxic lead, and the intrinsic phase instability of these materials.<sup>5–7</sup> Lead-free double perovskites with a stoichiometry of A<sub>2</sub>B<sup>III</sup>X<sub>6</sub> emerged as a possible alternative composition, where two [PbX<sub>3</sub>]<sup>2–</sup> octahedra are replaced by alternating corner-sharing [B<sup>I</sup>X<sub>6</sub>]<sup>5–</sup> and [B<sup>III</sup>X<sub>6</sub>]<sup>3–</sup> octahedra to avoid the use of divalent B-cations (Pb, Sn, Ge) in favor of the combination of more environmentally friendly B<sup>I</sup> and B<sup>III</sup> cations, which are less susceptible to oxidation.<sup>8–10</sup> In particular Cs<sub>2</sub>AgInCl<sub>6</sub> composition has attracted attention due to the

direct bandgap and broad emission with near-unity PL QY in the bulk crystal form, since a parity-forbidden transition can be changed to a parity-allowed one through the combination of B<sup>III</sup>-site doping and Bi<sup>3+</sup> and B<sup>I</sup>-site alloying with Na<sup>+</sup>.<sup>11,12</sup> There have been subsequent attempts to overcome the limited solubility of chlorine precursors and to establish strategies for the synthesis of colloidal Cs<sub>2</sub>AgInCl<sub>6</sub> NCs using either the anti-solvent precipitation method or the hot-injection approach, which adopted benzoyl chloride, 2-ethylhexanoyl chloride or hydrogen chloride and metal chlorides as chlorine precursors.<sup>13–15</sup> Notably, a trace amount of Bi<sup>3+</sup> doping (with a common feed ratio of ~1%) is necessary in their synthesis, which passivates surface defects and promotes radiative localization; otherwise, the broad emission from self-trapped excitons (STEs) can hardly be observed.<sup>16</sup> However, even after exhaustive optimization of reaction conditions during the hot injection procedure, the champion reported PL QY of Bi<sup>3+</sup>-doped Cs<sub>2</sub>AgInCl<sub>6</sub> NCs was barely above 11%.<sup>17</sup> B<sup>III</sup>-site co-doping was first proposed to realize special emission features originating from certain lanthanide co-dopants,<sup>18</sup> while the PL QYs in those studies were not evaluated.<sup>15,19</sup> Later, it was noticed that such co-doping can also efficiently enhance the optical performance of double-perovskite NCs. For example, using Bi<sup>3+</sup> and Ce<sup>3+</sup> (or Ni<sup>2+</sup>) as the co-doping pairs could endow Cs<sub>2</sub>Ag<sub>0.4</sub>Na<sub>0.6</sub>InCl<sub>6</sub> bulk crystals with PL QYs near unity.<sup>20</sup> Doping both Ce<sup>3+</sup> and Bi<sup>3+</sup> in Cs<sub>2</sub>AgInCl<sub>6</sub> NCs enhanced the localization of STEs to inhibit PL quenching,

<sup>a</sup>Department of Materials Science and Engineering, and Centre for Functional Photonics (CFP), City University of Hong Kong, 83 Tat Chee Avenue, Hong Kong S.A. R. 999077, P. R. China. E-mail: andrey.rogach@cityu.edu.hk

<sup>b</sup>College of Chemistry, Key Laboratory of Theoretical & Computational Photochemistry of Ministry of Education, Beijing Normal University, Beijing, 100875 P.R. China. E-mail: runlong@bnu.edu.cn

†Electronic supplementary information (ESI) available. See DOI: <https://doi.org/10.1039/d2nr04717a>

‡These two authors contributed equally to this research.

and achieved the highest PL QY of 26%.<sup>21</sup> The isovalent Bi<sup>III</sup>-site co-doping strategy was found to efficiently prevent the formation of uncoordinated chloride ions (and thus result in less Ag/In vacancies), which benefits the Jahn–Teller distortion of [AgCl<sub>6</sub>]<sup>5−</sup> octahedra for self-trapped emission in double perovskite NCs. The absence of the excess chloride ions at the surface of perovskite NCs further endows the capping oleic acid ligands with highly protonated carboxyl groups. Notably, the Bi<sup>3+</sup> and Te<sup>4+</sup> co-doping strategy has recently been applied to zero-dimensional metal halides such as Cs<sub>2</sub>SnCl<sub>6</sub> NCs and Cs<sub>2</sub>HfCl<sub>6</sub> bulk materials, resulting in STE emission with PL QYs of 28% and 70%, respectively.<sup>22,23</sup> However, they are not in perovskite families and require strongly confined photo-generated carriers for STE emissions, with the absence of free exciton emissions.<sup>24,25</sup> In contrast, the working performance of co-dopants in a connected metal halide octahedron matrix, together with the underlying mechanism of the formation of B-site vacancies, remained unexplored.

Here, a heterovalent Bi<sup>3+</sup> and Te<sup>4+</sup>-co-doping strategy was conducted in the Cs<sub>2</sub>AgInCl<sub>6</sub> NC system by an *in situ* surface treatment with oxygen vacancies on tellurium precursors in order to shed light on the formation of B-site vacancies and the stability of the nanoscale double perovskite structure. Both pristine (Cs<sub>2</sub>AgInCl<sub>6</sub> NCs doped with a feed ratio of 1% Bi, denoted as Cs<sub>2</sub>AgInCl<sub>6</sub>:0% Te, 1% Bi NCs) and co-doped NCs doped with a feed ratio of 1% Bi and *x*% Te (denoted as Cs<sub>2</sub>AgInCl<sub>6</sub>:*x*% Te, 1% Bi NCs, *x* = 1, 2, 4, 8, 12%) were synthesized for comparative studies. A champion PL QY of 34% for Cs<sub>2</sub>AgInCl<sub>6</sub>:8% Te, 1% Bi NCs at 591 nm was achieved as a result of the improved localization of STEs during radiative recombination, and it suppressed uncoordinated surface chlorine ions and silver/indium vacancies that work collectively together with acidic ligands to prevent the structural deterioration of perovskites under the electron beam during transmission electron microscopy (TEM) measurements, an indicator of greater structural robustness.

## Experimental details

### Chemicals and reagents

Cesium carbonate (Cs<sub>2</sub>CO<sub>3</sub>, 99.9%), anhydrous indium chloride (InCl<sub>3</sub>, 99.999%), bismuth chloride (BiCl<sub>3</sub>, 99.99%), silver nitrate (AgNO<sub>3</sub>, 99.8%), and oleic acid (OA, 90%) were purchased from Sigma Aldrich. *N*-hexane (99%), oleylamine (OLA, 80–90%), 1-octadecene (ODE, 90%), concentrated hydrochloric acid (HCl, 37%), methyl acetate (MeOAc, anhydrous, 99.5%), nitric acid (AR, 65–68%), tellurium dioxide (99.99%), zirconium dioxide (99%), titanium dioxide (99%), and germanium dioxide (99.99%) were purchased from Aladdin.

### Synthesis of Cs oleate

Cs<sub>2</sub>CO<sub>3</sub> (0.814 g), ODE (10 mL), and OA (2.5 mL) were loaded into a 50 mL three-neck flask followed by a degassing process under vacuum at 120 °C for 1 h. The mixture was heated under N<sub>2</sub> to 150 °C until the solution became clear. The resulting solu-

tion was cooled down naturally and stored in a refrigerator. A pre-heating process using a hot air dryer was necessary before use.

### Synthesis of Cs<sub>2</sub>AgInCl<sub>6</sub>:0% Te, 1% Bi NCs

AgNO<sub>3</sub> (61.1 mg), InCl<sub>3</sub> (79.6 mg), BiCl<sub>3</sub> (1.1 mg), ODE (14 mL), OA (1 mL), OLA (1 mL), and HCl (280 μL) were successively loaded into a 50 mL three-necked flask and preheated to 120 °C under vacuum for 1 h. The flask was flushed with Ar gas and then heated to 280 °C. 1 mL of hot (~100 °C) Cs oleate solution was rapidly injected under vigorous stirring for 10 s. The mixture was cooled down in a water bath (~25 °C) and centrifuged at 8000 rpm for 4 min; the precipitate was collected, redispersed in 3 mL of hexane, and centrifuged again at 5000 rpm for 4 min. The supernatant was collected, mixed with twice the volume of methyl acetate, and centrifuged at 10 000 rpm for 5 min to obtain a purified precipitate. The purification process was repeated twice, and the final precipitate was redispersed in hexane for further characterization.

### Synthesis of Bi,Te-co-doped Cs<sub>2</sub>AgInCl<sub>6</sub>:*x*% Te, 1% Bi NCs (*x*% = 1, 2, 4, 8 and 12%)

AgNO<sub>3</sub> (61.1 mg), BiCl<sub>3</sub> (1.1 mg), ODE (14 mL), OA (1 mL), OLA (1 mL), HCl (0.28 mL), and HNO<sub>3</sub> (30 μL) were loaded into a 50 mL three-necked flask. InCl<sub>3</sub> and tellurium dioxide powder were also added to the same flask in amounts of 78.0 and 0.6 mg (*x* = 1%), 77.2 and 1.3 mg (*x* = 2%), 75.6 and 2.6 mg (*x* = 4%), 72.4 and 5.2 mg (*x* = 8%), and 69.3 mg and 10.5 mg (*x* = 12%), respectively. The reaction and purification steps were conducted in the same way as described above. For the experiments where 8% of TeO<sub>2</sub> was replaced by inert dioxides, the feeding amounts of GeO<sub>2</sub>, ZrO<sub>2</sub>, and TiO<sub>2</sub> were 3.4 mg, 4.0 mg, and 2.6 mg, respectively.

### Characterization

Powder X-ray diffraction (XRD) measurements were conducted on a Rigaku Smartlab X-ray diffractometer. The optical diffuse reflectance spectra were collected on a Shimadzu UV 3600 UV/visible/IR spectrophotometer. The PL and photoluminescence excitation (PLE) spectra were recorded on an FLS920P spectrometer (Edinburgh Instruments). Absolute PL QYs were determined on the same spectrometer with the aid of an integrating sphere accessory with its inner face coated with BENFLEC. Quinine sulfate in 0.1 M H<sub>2</sub>SO<sub>4</sub> with a known PL QY of 58% was used as a reference to confirm the measurement accuracy. Time-resolved PL decays were measured on the same spectrometer using a time-correlated single-photon counting system. X-ray photoelectron spectroscopy (XPS) was performed on a PHI model 5802 instrument. Fourier-transform infrared (FTIR) and Raman spectra were collected on a PerkinElmer FTIR spectrophotometer and a WITec Alpha300R confocal Raman imaging system equipped with a 532 nm laser, respectively. Transmission electron microscopy (TEM) was performed on a JEOL 2100F instrument. Scanning electron microscopy (SEM) and energy dispersive X-ray spectroscopy (EDS) measurements were performed on an FEI Quanta 250 instrument. Elemental

analysis was carried out using inductively coupled plasma atomic emission spectroscopy (ICP-AES).

### Calculation of the average PL lifetime, radiative decay rate, Huang–Rhys factor, and exciton binding energy

The average (effective) PL lifetimes ( $\tau_{\text{avg}}$ ) were calculated using the following equation:<sup>26</sup>

$$\tau_{\text{avg}} = \frac{\int_0^{\infty} tI(t)dt}{\int_0^{\infty} I(t)dt}.$$

The radiative decay rate ( $K_r$ ) for an ideal system of identical perovskite NCs was determined using the following equation:<sup>27</sup>

$$\frac{1}{K_r} = \tau_r = \frac{\tau_{\text{avg}}}{QY}.$$

The thermal evolution of the PL full width half maximum (FWHM) was applied to determine the Huang–Rhys factor,  $S$ , using the following equation:<sup>12</sup>

$$\text{FWHM}(T) = 2.36\sqrt{S\hbar\omega_{\text{phonon}}}\sqrt{\coth\left(\frac{\hbar\omega_{\text{phonon}}}{2k_B T}\right)}$$

where  $\hbar\omega_{\text{phonon}}$  represents the frequency of phonons involved in the relaxation of the band edge excitation and  $k_B$  is the Boltzmann constant ( $8.62 \times 10^{-2}$  meV K<sup>-1</sup>).

The exciton binding energy ( $E_B$ ) was derived using the following equation:<sup>28</sup>

$$I(T) = \frac{I_0}{1 + Ae^{-E_B/k_B T}}$$

where  $I_0$  is the PL intensity at 0 K,  $k_B$  is the Boltzmann constant, and  $A$  is a pre-exponential constant factor, determined by fitting the temperature dependent PL intensity.

## Computational details

Pristine Cs<sub>2</sub>AgInCl<sub>6</sub> was modeled with a 160-atom  $2 \times 2 \times 1$  supercell in the cubic phase, with an experimental lattice parameter of 10.48 Å.<sup>29</sup> The Bi-doped system was created by substituting one Bi atom for an In atom (Bi → In). The Bi/Te-co-doped systems were formed by replacing one Te atom at a Ag-site (Te → Ag) or an In-site (Te → In). The vacancy defect systems were simulated by removing an Ag or In atom from the Cs<sub>2</sub>AgInCl<sub>6</sub> supercell. The geometry optimization was carried out using the Vienna *ab initio* simulation package (VASP),<sup>30</sup> adopting the Perdew–Burke–Ernzerhof (PBE) functional<sup>31</sup> to describe electronic exchange–correlation interactions and the projector-augmented wave approach<sup>32</sup> to treat ion–electron interactions. The  $2 \times 2 \times 4$  Monkhorst–Pack  $k$ -point sampling<sup>33</sup> was used for geometry optimization. The geometry optimization was considered as converged when ion forces became less than  $10^{-3}$  eV Å<sup>-1</sup>. The van der Waals interactions were described using the Grimme DFT-D3 method with Becke–Johnson damping.<sup>34,35</sup>

### Defect formation energy calculation

The energy  $E_{\text{form}}(D, q)$  for the formation of a defect  $D$  in a charge state  $q$  was calculated as:<sup>36</sup>

$$E_{\text{form}}(D, q) = E(D, q) - E(\text{host}) + \sum n_i E_i + q(\Delta E_{\text{fermi}} + E_{\text{VBM}}).$$

Here,  $E(D, q)$  is the total energy of a supercell with defect  $D$  in the charge state  $q$ ;  $E(\text{host})$  is the total energy of the supercell without the defect;  $n_i$  is the number of removed atoms of element  $i$ ;  $E_i$  is the energy of an atom of the  $i$  element in its bulk phase;  $\Delta E_{\text{fermi}}$  is the energy difference between the valence band maximum (VBM) and the Fermi energy;<sup>37</sup>  $E_{\text{VBM}}$  is the VBM energy of the host supercell without any defects. In the present study,  $q$  equals 0 for all defects, and therefore, the last term of the above equation vanishes.

## Results and discussion

As shown in Fig. 1a, the absorption intensity at around 300 nm was suppressed while introducing 1%, 2%, or 12% TeO<sub>2</sub> into the 1% Bi-doped Cs<sub>2</sub>AgInCl<sub>6</sub> (hereinafter referred to as Cs<sub>2</sub>AgInCl<sub>6</sub>:0% Te, 1% Bi) NCs indicating an undesirably high degree of free Te<sup>4+</sup> cations that participated in the aliovalent doping and compromised the quality of the crystal lattice. It increased while being doped with an adjusted feed ratio of 4% and 8% TeO<sub>2</sub>, when the reduced doping amount of Te<sup>4+</sup> favored the formation of tellurium oxides in the presence of trace amounts of hydrogen chloride and hydrogen nitrate. A slightly red-shifted optical bandgap derived from Tauc plots (inset in Fig. 1a) was also observed, probably arising from lattice defects while considering the greatly inhibited deep defects visible from the enlarged absorption tails (see Fig. S1†).<sup>38</sup> However, similar to the dopant-free Cs<sub>2</sub>AgInCl<sub>6</sub> NCs, for the case of feeding the system with 8% tellurium precursors (*i.e.* without any Bi co-dopants), the self-trapped emission could not be observed, although there was defect-related blue emission peaking at 438 nm (Fig. S2†).<sup>16,17</sup> Fig. 1b summarizes the evolution of the absorption peak and optical bandgap trends which occur upon doping. In comparison with Cs<sub>2</sub>AgInCl<sub>6</sub>:0% Te, 1% Bi NCs, the absorption peak of Cs<sub>2</sub>AgInCl<sub>6</sub>:8% Te, 1% Bi displays the biggest difference of 2 nm (18 meV) for the absorption peak, while its optical bandgap becomes greatly reduced to 46 meV, suggesting a higher level of incorporation of dopants or passivation of surface-related defects or both. PL excitation (PLE) and PL spectra in Fig. 1c show that the samples with different Te amounts have the same PLE maximum at 370 nm which reveals their common self-trapped states that turn into a broad PL emission. As shown in Fig. 1d, a slight red shift of self-trapped emission is obtained depending on the feeding level of the Te precursor. Compared to the pristine Cs<sub>2</sub>AgInCl<sub>6</sub>:0% Te, 1% Bi NCs (PL QY: 12% at 589 nm), Cs<sub>2</sub>AgInCl<sub>6</sub>:8% Te, 1% Bi NCs show a tripled PL QY of 34% at 591 nm, outperforming other B<sup>III</sup>-site doped counterparts (Table S1†). The photo-

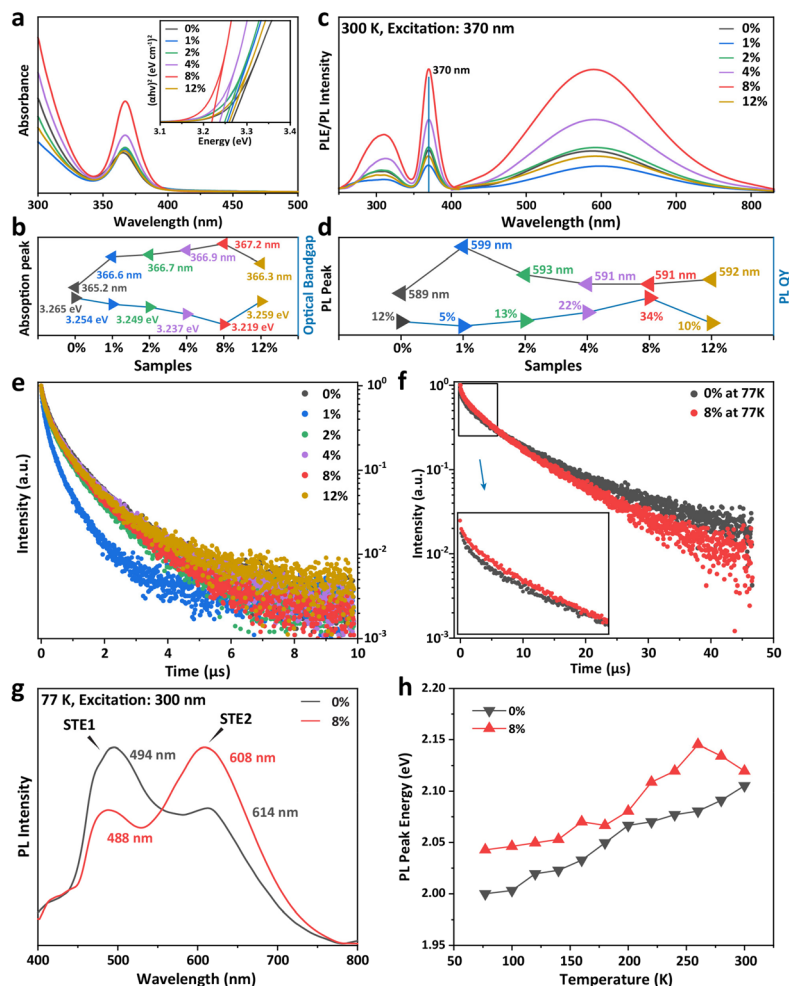


**Fig. 1** Optical characteristics of 1% Bi-doped ( $\text{Cs}_2\text{AgInCl}_6:0\% \text{ Te}, 1\% \text{ Bi}$ ) and 1% Bi,  $x\%$  Te-co-doped ( $\text{Cs}_2\text{AgInCl}_6:x\% \text{ Te}$ ) NCs: (a) absorption spectra with the corresponding Tauc plots given in the inset; (b) dependence of the absorption peak position (upper curve) and optical bandgap (lower curve) on the Te dopant amount in the samples; (c) PLE and PL spectra; (d) dependence of the PL peak position (upper curve) and PL QY (lower curve) on the Te dopant amount in the samples; (e) PL decay curves recorded at room temperature under 375 nm laser excitation. Frames (f and g) show additional optical characteristics for  $\text{Cs}_2\text{AgInCl}_6:0\% \text{ Te}, 1\% \text{ Bi}$  and  $\text{Cs}_2\text{AgInCl}_6:8\% \text{ Te}, 1\% \text{ Bi}$  NCs: (f) PL decay curves recorded at 77 K under 375 nm laser excitation, (g) PL spectra at 77 K using an excitation wavelength of 300 nm, and (h) temperature-dependent PL peak energy evolution of the two samples.

graphs in Fig. S3† further demonstrate the improved emission of the co-doped samples while diluting 200  $\mu\text{l}$  of the perovskite solution in 2 ml of hexane. It is noted that  $\text{Cs}_2\text{AgInCl}_6:8\% \text{ Te}, 1\% \text{ Bi}$  has the minimum difference between the optical bandgap and the self-trapped state, indicating a more efficient energy release channel for excitons during the radiative recombination, which further promotes their optical performance.

According to the time-resolved PL decay curves recorded under 375 nm laser excitation presented in Fig. 1e, long PL lifetimes, as a feature of STE, are found for all samples (measured in hexane solution). The average PL lifetime of  $\text{Cs}_2\text{AgInCl}_6:x\%, 1\% \text{ Bi}$  Te NCs at room temperature is found to be 1.06  $\mu\text{s}$  ( $x = 0\%$ ), 0.63  $\mu\text{s}$  ( $x = 1\%$ ), 0.94  $\mu\text{s}$  ( $x = 2\%$ ), 1.11  $\mu\text{s}$  ( $x = 4\%$ ), 0.96  $\mu\text{s}$  ( $x = 8\%$ ), and 1.05  $\mu\text{s}$  ( $x = 12\%$ ), respectively. The detrimental effect on shortening the average PL lifetime while introducing 1%  $\text{TeO}_2$  could be attributed to a higher

degree of  $\text{Te}^{4+}$  doping during exposure to concentrated HCl and  $\text{HNO}_3$  solution. Because of the increase in the feed ratio of  $\text{TeO}_2$ , the Te–O bond can hardly fully dissociate and thus triggers the formation of other oxides like  $\text{Te}_2\text{O}_3\text{Cl}_2$  and  $\text{R}_2\text{TeO}$ , surface oxygen defects of which provide an *in situ* force to overcome the presence of excessive chlorine ions surrounding  $\text{Cs}_2\text{AgInCl}_6$  NCs, which improves their crystallinity and PL lifetime. A study on the radiative mechanism was further conducted. As presented in Table S2,† a much more efficient radiative decay process was found in  $\text{Cs}_2\text{AgInCl}_6:8\% \text{ Te}, 1\% \text{ Bi}$  NCs (radiative recombination rate  $K_r$  equal to  $3.54 \times 10^5 \text{ s}^{-1}$ ) though  $\text{Cs}_2\text{AgInCl}_6:0\% \text{ Te}, 1\% \text{ Bi}$  NCs and  $\text{Cs}_2\text{AgInCl}_6:12\% \text{ Te}, 1\% \text{ Bi}$  NCs possess a slightly longer average lifetime. Low-temperature PL lifetime measurements at 77 K indicate that  $\text{Cs}_2\text{AgInCl}_6:0\% \text{ Te}, 1\% \text{ Bi}$  NCs and  $\text{Cs}_2\text{AgInCl}_6:8\% \text{ Te}, 1\% \text{ Bi}$  NCs have average PL lifetimes of 10.7  $\mu\text{s}$  and 8.77  $\mu\text{s}$ , respect-



ively. However, as shown in Fig. 1f, a longer PL lifetime component can be observed at the early decay stage of  $\text{Cs}_2\text{AgInCl}_6$ :8% Te,1% Bi NCs which may indirectly point to a long lifetime of STEs alongside an initial fast radiative decay process conferring a higher PL QY on the system.

Significantly, multiple STE states (marked as STE1 and STE2 in Fig. 1g) appeared when using an excitation wavelength of 300 nm at 77 K.  $\text{Cs}_2\text{AgInCl}_6$ :8% Te,1% Bi has dominant STE2 emission while  $\text{Cs}_2\text{AgInCl}_6$ :0% Te,1% Bi shows stronger emission from STE1, suggesting a preferred radiative recombination channel with a deeper bandgap and fewer nonradiative recombination centers in the former sample which in turn benefits its self-trapped emission at room temperature. On heating up the two samples, the evolution of their PL peak energy shows an increasing trend due to thermal expansion of their lattices that usually causes a blue shift in the PL spectra (Fig. 1h). However, an obvious reduction in the PL peak energy occurs above 260 K for  $\text{Cs}_2\text{AgInCl}_6$ :8% Te,1% Bi NCs, which signifies the dominant effect of electron–phonon coupling over lattice dilation in this range. Fig. S4† shows the thermal evolution of the PL full width at half maximum (FWHM) and the temperature-dependent integrated PL intensity of the two samples. It further demonstrates the advantages of

$\text{Cs}_2\text{AgInCl}_6$ :8% Te,1% Bi NCs, which possess a higher exciton binding energy of  $45.9 \pm 7.6$  meV and a Huang–Rhys factor of  $70.4 \pm 6.6$  (indicating quite strong phonon coupling) while the respective values for  $\text{Cs}_2\text{AgInCl}_6$ :0% Te,1% Bi NCs are  $41.4 \pm 6.6$  meV for the exciton binding energy and  $52.4 \pm 2.6$  for the Huang–Rhys factor.

Study of the NC size and structure was conducted to further evaluate the effectiveness of co-doping bismuth and tellurium ions. As seen from the TEM images given in Fig. 2a–f, rather monodisperse cubic-shaped NCs with an average edge size of  $\pm 10$  nm for  $\text{Cs}_2\text{AgInCl}_6$ :0% Te,1% Bi and  $\pm 9$  nm for Bi/Te co-doped NCs were produced. More TEM images of  $\text{Cs}_2\text{AgInCl}_6$ :x % Te,1% Bi NCs with a wider field of vision are provided in Fig. S5.† Notably, multiple dark spots belonging to metallic silver appeared on each  $\text{Cs}_2\text{AgInCl}_6$ :0% Te,1% Bi NC, demonstrating its limited structural stability under electron beam irradiation in TEM, although silver particles could form under certain synthesis as well.<sup>17,39</sup> In contrast, those spots tended to fade away with an increasing amount of tellurium precursors and were remarkably absent when the Te feeding ratio reached 8%, demonstrating the greatly improved lattice crystallinity and far better structural stability under an electron beam. The crystallinity of the perovskite NCs took a turn for the worse,

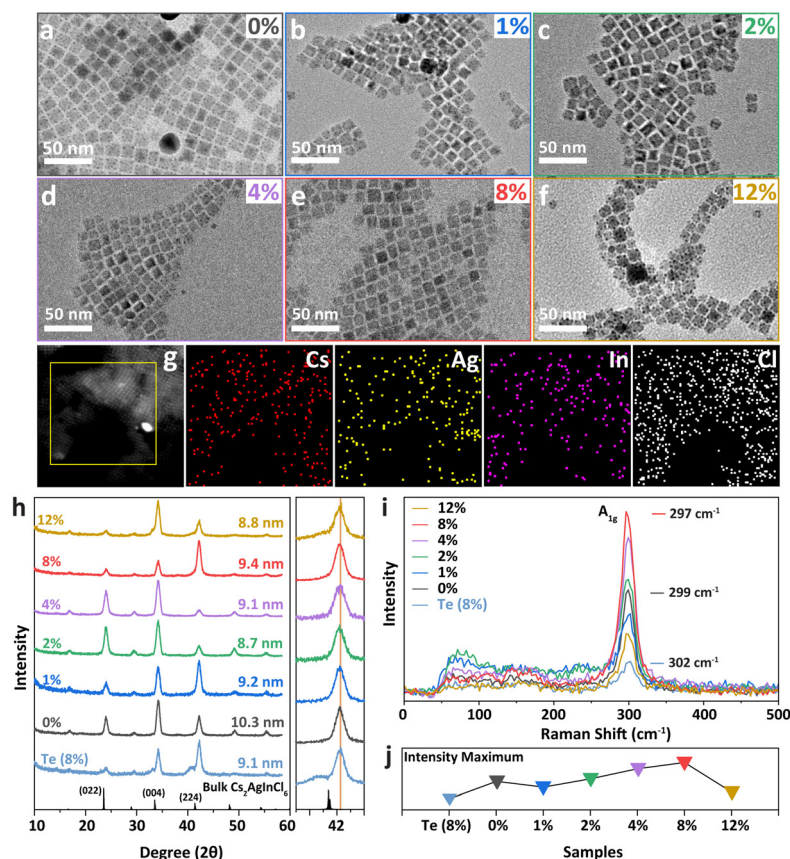


**Fig. 2** (a–f) TEM images of  $\text{Cs}_2\text{AgInCl}_6$ :x% Te,1% Bi NCs ( $x = 0, 1, 2, 4, 8, 12$ ); (g) STEM-HAADF image and the corresponding elemental mapping images for Cs, Ag, In and Cl of  $\text{Cs}_2\text{AgInCl}_6$ :8% Te,1% Bi NCs, acquired from the yellow-boxed area; (h) XRD patterns with an enlarged diffraction peak from the (224) lattice plane shown separately on the right side; (i) Raman spectra, and (j) a summary of the Raman intensity from the  $A_{1g}$  mode vibration of  $\text{Cs}_2\text{AgInCl}_6$ :x% Te,1% Bi and  $\text{Cs}_2\text{AgInCl}_6$ : 8% Te NCs (denoted as Te (8%) on frames h–j).

however, on reaching an excessive Te feeding ratio of 12%, according to the reappearance of the dark spots in Fig. 2f. Fig. 2g presents the scanning TEM image of  $\text{Cs}_2\text{AgInCl}_6$ :8% Te,1% Bi NCs taken under the high-angle annular dark-field (STEM-HAADF) mode, and the corresponding elemental mapping images in which all the primary elements in the perovskite host (Cs, Ag, In and Cl) can be observed clearly. XRD patterns in Fig. 2h present three main peaks corresponding to the typical lattice diffraction of bulk  $\text{Cs}_2\text{AgInCl}_6$  (ICSD 1927876), though the intensity of the dominant diffraction peaks varies in different samples, revealing that the presence of tellurium may influence the growth and crystallization of perovskite NCs to a certain degree. As presented in the enlarged diffraction peaks from the (224) lattice plane (Fig. 2h, right side), no obvious shift could be observed which can be attributed to the limited incorporation of  $\text{Te}^{4+}$  (111 pm radius) dopants. A similar phenomenon was also found in  $\text{Bi}^{3+}$  (117 pm) and  $\text{Er}^{3+}$  (103 pm) co-doped  $\text{Cs}_2\text{AgInCl}_6$  bulk double perovskites.<sup>15</sup> Similar to the TEM results, average sizes of around 9 nm for the NCs in Bi/Te-co-doped samples and 10.3 nm for  $\text{Cs}_2\text{AgInCl}_6$ :0% Te,1% Bi NCs were derived from XRD patterns according to the Scherrer formula. The suppressed size of Bi/Te-co-doped samples can be ascribed to the presence of tellurium dopants, as proved by the similar smaller size (~9 nm) of 8% tellurium single-doped (no Bi co-doping applied)  $\text{Cs}_2\text{AgInCl}_6$ : 8% Te NCs, which are marked in light blue in Fig. 2h.

The Raman spectra further demonstrated the effectiveness of the co-doping strategy with proper feeding ratios. As shown in Fig. 2i, all samples possessed a typical and dominant  $\text{A}_{1g}$  Raman mode at around  $300\text{ cm}^{-1}$  which corresponds to the stretching vibration of metal halide octahedra and relates

mostly to the  $[\text{AgCl}_6]^{5-}$  octahedron in the case of  $\text{Cs}_2\text{AgInCl}_6$  due to the high strain on the Ag–Cl bonds compared to that on the Bi/In–Cl bonds.<sup>40</sup> The  $\text{A}_{1g}$  mode of  $\text{Cs}_2\text{AgInCl}_6$ :8% Te,1% Bi NCs locates at  $297\text{ cm}^{-1}$  and shows a shift toward lower frequency in comparison with that of  $\text{Cs}_2\text{AgInCl}_6$ :0% Te,1% Bi ( $299\text{ cm}^{-1}$ ), suggesting that  $[\text{AgCl}_6]^{5-}$  octahedra are under tensile strain, or longer Ag–Cl bond lengths are achieved due to the presence of tetravalent  $\text{Te}^{4+}$  ions that could influence the state of neighboring octahedra. It is noted that  $\text{Cs}_2\text{AgInCl}_6$ :8% Te NCs (no Bi co-doping; the sample denoted as Te (8%) in Fig. 2i) have an  $\text{A}_{1g}$  mode at  $302\text{ cm}^{-1}$  pointing to lattice shrinkage in these NCs which can be attributed to intrinsic defects and poor crystallinity. As summarized in Fig. 2j, the  $\text{A}_{1g}$  mode of  $\text{Cs}_2\text{AgInCl}_6$ :8% Te,1% Bi NCs has the highest peak intensity which further demonstrates improved crystallinity upon co-doping with a proper amount of Bi and Te ions into the  $\text{Cs}_2\text{AgInCl}_6$  host.

FTIR measurements were conducted to study the surface states and ligand coordination of Te-doped perovskite NCs. As shown in Fig. 3a, after the reaction at a high temperature of  $280\text{ }^\circ\text{C}$  and a triple purification process, the broad O–H stretching vibration from  $\text{H}_2\text{O}$  molecules at around  $3500\text{ cm}^{-1}$  could be effectively suppressed in  $\text{Cs}_2\text{AgInCl}_6$ :x% Te,1% Bi ( $x = 0, 1, 2, 4, 8$ ) NCs, along with the appearance of an N–H stretching vibration at around  $3200\text{ cm}^{-1}$ . The asymmetric  $\nu_{\text{as}}(\text{COO}^-)$  vibration demonstrates a shift toward lower frequencies – from  $1583\text{ cm}^{-1}$  ( $\text{Cs}_2\text{AgInCl}_6$ :0% Te,1% Bi NCs) to  $1578\text{ cm}^{-1}$  ( $\text{Cs}_2\text{AgInCl}_6$ :1% Te,1% Bi NCs) and  $1580\text{ cm}^{-1}$  ( $\text{Cs}_2\text{AgInCl}_6$ :x% Te,1% Bi NCs,  $x = 2, 4, 8$ ), revealing a higher degree of protonation of the carboxyl group that coordinates with the double perovskite surface by hydrogen bonding.<sup>21</sup> When the tellurium feed ratio increases to 12%, the trend largely reverses,

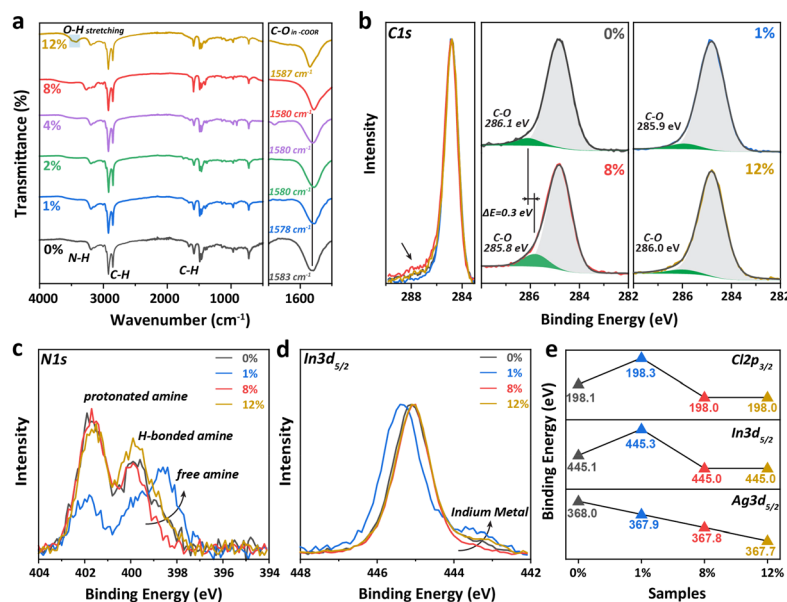


**Fig. 3** (a) FTIR spectra, XPS spectra of (b) C 1s, (c) N 1s, and (d) In 3d core levels, and (e) a summary of changes on the XPS peaks of Cl 2p, In 3d, and Ag 3d core levels of  $\text{Cs}_2\text{AgInCl}_6$ :x% Te,1% Bi NCs ( $x = 0, 1, 2, 4, 8, 12$ ).

accompanied by an obvious O–H stretching vibration at around  $3500\text{ cm}^{-1}$ , as a result of defects or vacancies that affect the nucleation and growth of perovskites and lead to undesired changes in the lattice crystallinity. From the perspective of the binding energies, the X-ray photoelectron spectra (XPS) of the C 1s core level in Fig. 3b demonstrate weaker C–O bonding of  $\text{Cs}_2\text{AgInCl}_6$ :1% Te, 1% Bi NCs (285.9 eV) and  $\text{Cs}_2\text{AgInCl}_6$ :8% Te, 1% Bi NCs (285.8 eV) than that of  $\text{Cs}_2\text{AgInCl}_6$ :0% Te, 1% Bi NCs (286.1 eV), in accordance with the FTIR results that demonstrate enhanced coordination between the perovskite surface and oleic acid ligands. Though a relatively higher binding energy of 286.0 eV was achieved,  $\text{Cs}_2\text{AgInCl}_6$ :12% Te, 1% Bi NCs still performed worse, which can be attributed to the undesired level of crystallinity and hydrogen-bonded  $\text{H}_2\text{O}$  molecules at the NC surface and/or near carboxyl groups after introducing excess tellurium precursors. We note that the integrated area ratio between C–O and C–C bonding decreases from 8.2% ( $\text{Cs}_2\text{AgInCl}_6$ :0% Te, 1% Bi NCs) to 5.6% ( $\text{Cs}_2\text{AgInCl}_6$ :1% Te, 1% Bi NCs), revealing a loss of surface ligands; nevertheless, the same ratio is almost doubled to 12.6% while continuously increasing the tellurium dopants ( $\text{Cs}_2\text{AgInCl}_6$ :8% Te, 1% Bi NCs), which points to an increasing number of oleic acid ligands involved in stabilization at the surface of the latter sample as a result of well-suppressed surface defects and Ag/In vacancies. Accordingly, the XPS-derived data presented in Table S3† show that  $\text{Cs}_2\text{AgInCl}_6$ :8% Te, 1% Bi NCs have much better balanced In:Ag and Cl:In ratios of 1.1 and 5.9 while those of  $\text{Cs}_2\text{AgInCl}_6$ :0%, 1% and 12% Te, 1% Bi NCs are around 1.2 for the In:Ag ratio and 6.4 for the Cl:Ag ratio, respectively, revealing effectively suppressed uncoordinated chlorine ions in the sample with 8% Te. At the same time, the ICP-AES study showed a slightly declining Te/In ratio tracking from 0.002 for  $\text{Cs}_2\text{AgInCl}_6$ :1% Te, 1% Bi NCs to 0.002 for  $\text{Cs}_2\text{AgInCl}_6$ :8% Te, 1% Bi and 0.001 for  $\text{Cs}_2\text{AgInCl}_6$ :12% Te, 1% Bi in spite of the experimental method's relatively low sensitivity for semi-metals like Te. According to the ICP-AES results, the estimated Bi/In doping ratio in those samples can be given as around 0.005. Hence, the optical changes caused by different tellurium feed ratios primarily arise from the use of excess  $\text{TeO}_2$  that has not been dissolved by hydrogen chloride and nitric acid, but remained present in the reaction mixture in a possible form of  $\text{TeO}_2$  and some tellurium complexes such as  $\text{R}_2\text{TeO}$  or  $\text{Te}_2\text{O}_3\text{Cl}_2$  (Fig. S6†) to confine excess chlorine ions and regulate the nucleation and growth of the double perovskite NC host physically and chemically. Those tellurium oxides are further impactful given their surface oxygen vacancies, which are naturally present in every oxide in the form of Schottky or Frenkel defects,<sup>41</sup> facilitating the adsorption of surplus chlorine ions to counteract the pull from  $\text{Cs}_2\text{AgInCl}_6$  NCs, which are often rich in Ag/In vacancies and excessive  $\text{Cl}^-$ . In order to evaluate the effectiveness of external oxygen vacancies, 8% of inert dioxides including  $\text{GeO}_2$ ,  $\text{ZrO}_2$ , and  $\text{TiO}_2$ , together with 1% Bi-doping, were used to replace  $\text{TeO}_2$ , respectively. A similar trend is found in their absorption spectra (Fig. S7†) presenting an obvious enhancement of the

excitonic peak with a slight red shift because of the improving crystallinity upon suppression of excessive chlorine ions. The feature also helps to improve PL QYs to 14%, 16% and 17% for  $\text{GeO}_2$ ,  $\text{ZrO}_2$ , and  $\text{TiO}_2$  treated samples, respectively, proving the positive effects of external oxygen vacancies.

As is seen from the XPS spectra of the N 1s core level in Fig. 3c, the signal corresponding to free amine is almost absent in  $\text{Cs}_2\text{AgInCl}_6$ :8% Te, 1% Bi NCs due to restrained lattice defects. Accordingly, the XPS spectra of the In  $3d_{5/2}$  core level in Fig. 3d demonstrate a significantly suppressed indium metal composition at around 443.8 eV in  $\text{Cs}_2\text{AgInCl}_6$ :8% Te, 1% Bi NCs. Fig. 3e summarizes the binding energy evolution of the four samples showing a declining binding energy of the Ag  $3d_{5/2}$  region of  $\text{Cs}_2\text{AgInCl}_6$ :0% Te, 1% Bi (368.0 eV),  $\text{Cs}_2\text{AgInCl}_6$ :1% Te, 1% Bi (367.9 eV),  $\text{Cs}_2\text{AgInCl}_6$ :8% Te, 1% Bi (367.8 eV) and  $\text{Cs}_2\text{AgInCl}_6$ :12% Te, 1% Bi (367.7 eV) NCs. This means that the amount of metallic silver reduces after feeding in more  $\text{TeO}_2$  precursor while considering the reversed shift in the binding energy of oxidized silver.<sup>42,43</sup> Due to the effective incorporation of tetravalent tellurium dopants, the In–Cl binding energy decreases from 445.1 eV for  $\text{Cs}_2\text{AgInCl}_6$ :0% Te, 1% Bi NCs to 445.0 eV for  $\text{Cs}_2\text{AgInCl}_6$ :8% Te, 1% Bi and  $\text{Cs}_2\text{AgInCl}_6$ :12% Te, 1% Bi NCs. In contrast, the unusual increase in the binding energy in the Cl 2p and In  $3d_{5/2}$  regions of  $\text{Cs}_2\text{AgInCl}_6$ :1% Te, 1% Bi NCs can be observed due to high concentrations of lattice defects such as the presence of indium metal.

The Bi/Te-co-doped double perovskite NCs could maintain a colloidal stability suitable for a spin coating treatment, even when stored in the refrigerator for around one month, as examined by SEM mapping (Fig. S8†) on the resulting films. Apart from the improved colloidal stability,  $\text{Cs}_2\text{AgInCl}_6$ :8% Te, 1% Bi NCs retained ~70% of the initial PL intensity after one month, while  $\text{Cs}_2\text{AgInCl}_6$ :0% Te, 1% Bi lost over 60% of the original PL intensity during the storage (Fig. S9†). As is seen from the XRD patterns shown in Fig. 4a, all samples stored for around one month retained their typical crystal structure without the presence of impurity phases, showing their high stability in comparison with that of lead/tin halide counterparts, except for  $\text{Cs}_2\text{AgInCl}_6$ :12% Te, 1% Bi and  $\text{Cs}_2\text{AgInCl}_6$  NCs solely doped by the 8% tellurium precursor, where the solutions of both were observed to have severely precipitated. Notably, the (022) lattice plane replaced the (224) or (004) lattice plane as the most intense and dominated the crystalline orientation in  $\text{Cs}_2\text{AgInCl}_6$ :8% Te, 1% Bi NCs, which suggests that the lattice reconstruction process could also occur in double perovskite NCs. At the same time, the diffraction peak from the (022) plane experiences a shift from  $24.00^\circ$  for  $\text{Cs}_2\text{AgInCl}_6$ :0% Te, 1% Bi NCs to  $23.95^\circ$  for  $\text{Cs}_2\text{AgInCl}_6$ :8% Te, 1% Bi NCs due to the different sizes of  $\text{Te}^{4+}$  (111 ppm),  $\text{Bi}^{3+}$  (117 ppm), and  $\text{In}^{3+}$  (94 ppm) that lead to a certain level of lattice expansion on their incorporation.

Theoretical calculations on defect (silver/indium vacancies) formation energies were performed for dopant-free and Bi-doped (replacing In)  $\text{Cs}_2\text{AgInCl}_6$  and that co-doped with Bi (replacing In) and Te (replacing Ag or In), and the results are

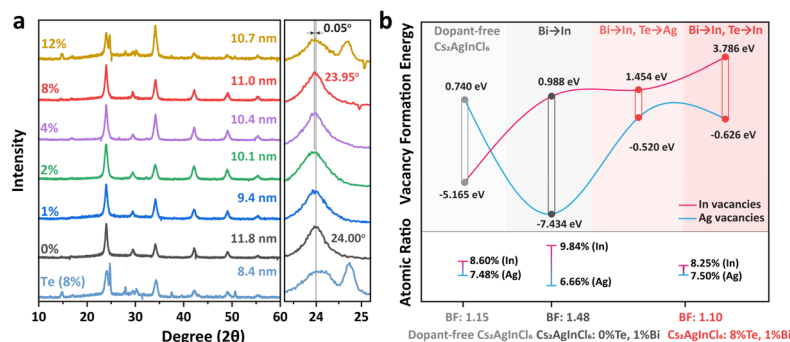


**Fig. 4** (a) XRD pattern of  $\text{Cs}_2\text{AgInCl}_6$ : $x\%$ Te,1%Bi NCs ( $x = 0, 1, 2, 4, 8, 12$ ) and  $\text{Cs}_2\text{AgInCl}_6$  NCs solely doped with 8% Te without any Bi co-doping, that is Te (8%), stored for around 1 month in a refrigerator, with an enlarged diffraction peak from the (004) lattice plane shown on the right side. (b) Calculated defect formation energies of B-site vacancies and In/Ag atomic ratios derived from SEM-EDS data for dopant-free  $\text{Cs}_2\text{AgInCl}_6$ ,  $\text{Cs}_2\text{AgInCl}_6$ :0%Te,1%Bi, and  $\text{Cs}_2\text{AgInCl}_6$ :8%Te,1%Bi NCs. BF appearing on the X-axis is the balance factor (BF) which is defined as the atomic ratio of In divided by that of Ag, and thus indicates the amount of silver vacancies.

presented in Fig. 4b; this was done in order to establish whether tellurium doping could benefit the perovskite lattice in terms of increasing the formation energies of Ag/In vacancies. The simulation details are outlined in the ESI.† According to these calculations, the generation of an indium vacancy ( $V_{\text{In}}$ ) in  $\text{Cs}_2\text{AgInCl}_6$  requires  $-5.165$  eV, while this value increases to  $0.988$  eV after Bi-doping at the In-site, which would bring down the formation energy of the silver vacancy ( $V_{\text{Ag}}$ ) from  $0.740$  eV to  $-7.434$  eV, thereby leading to a significant lattice distortion and an accumulation of excess chlorine ions, thus resulting in low PL QYs of perovskite NCs. This conclusion is further supported by In/Ag atomic ratios derived from SEM-energy dispersive X-ray spectroscopy (EDS) data, which are shown at the bottom of Fig. 4b. Here, the balance factor (BF) is defined as the atomic ratio of In divided by that of Ag, which denotes the concentration of silver vacancies. The derived BF value for 1% Bi-doped ( $\text{Cs}_2\text{AgInCl}_6$ :0%Te,1%Bi) NCs (1.48) is remarkably higher than for dopant-free  $\text{Cs}_2\text{AgInCl}_6$  (1.15), revealing a highly unbalanced Ag/In ratio after introducing bismuth dopants, which is essential for self-trapped emissions.<sup>44,45</sup> This is greatly remedied in the Te/Bi-co-doped NCs, which show a low BF value of 1.10 for  $\text{Cs}_2\text{AgInCl}_6$ :8%Te,1%Bi as a result of the hindered formation of Ag/In vacancies in the perovskite lattices. The theoretical results also show that on co-doping Te at an Ag-site or an In-site, the overall  $V_{\text{In}}$  and  $V_{\text{Ag}}$  values are effectively enhanced to  $1.454$  eV and  $-0.520$  eV or  $3.786$  eV and  $-0.626$  eV, respectively, which contributes to the reduction of any defect amounts in the Te-co-doped perovskite NCs.

## Conclusions

In conclusion,  $\text{Bi}^{3+}$  and  $\text{Te}^{4+}$  cations were successfully co-doped into a lead-free double perovskite  $\text{Cs}_2\text{AgInCl}_6$  NC host during a modified hot-injection process. The tellurium precursor was found to dope  $\text{Te}^{4+}$  cations into the perovskite lattice and to restrain the formation of silver and indium vacancies.

In excess, the precursor would produce  $\text{TeO}_2$ ,  $\text{Te}_2\text{O}_3\text{Cl}_2$ ,  $\text{R}_2\text{TeO}$ , or all three of them, which confined undesired chlorine ions on oxygen vacancies to counteract the pull from the  $\text{Cs}_2\text{AgInCl}_6$  host, which in turn resulted in improved coordination with surface oleic acid ligands. As a result,  $\text{Cs}_2\text{AgInCl}_6$  NCs co-doped with 1% Bi and 8% Te achieved a champion PL QY of 34% at 591 nm while their 1% Bi-doped counterparts showed a much lower PL QY of 11% at 589 nm. According to Table S1,† such a PL QY of 34% is also the champion value among all double perovskite  $\text{Cs}_2\text{AgInCl}_6$ -based NCs reported so far. Theoretical calculations further suggest the important role of tellurium dopants in decreasing silver and indium vacancies. Improved crystallinity also ensured better stability of the  $\text{Cs}_2\text{AgInCl}_6$  NCs, which could retain over 70% of its original PL intensity after storage for around 1 month, though accompanied by a possible lattice reconstruction process. The synergetic co-doping and surface treatment strategies demonstrated in this study are important in the context of producing high-performance double perovskite nanocrystals for optoelectronic devices, especially when considering that the practical applications of such lead-free perovskite materials still lag behind their lead halide counterparts.

## Author contributions

Shixun Wang: conceptualization, methodology, validation, investigation, and writing – original draft. Ran Shi: methodology, validation, investigation, and writing – theoretical analysis. Bing Tang: investigation. Yuan Xiong: investigation. Arsenii Portniagin: investigation. Xin Zhao: investigation. Stephen V. Kershaw: investigation, writing – review & editing. Run Long: resources, supervision, writing – review & editing. Andrey L. Rogach: resources, supervision, writing – review & editing.

## Conflicts of interest

The authors declare no competing financial interest.



## Acknowledgements

We acknowledge the financial support from the Research Grant Council of Hong Kong (C7035-20G) and from the Croucher Foundation of Hong Kong. R. L. is grateful to the Beijing Municipal Natural Science Foundation (2212031).

## References

- 1 A. Dey, J. Ye, A. De, E. Debroye, S. K. Ha, E. Bladt, A. S. Kshirsagar, Z. Wang, J. Yin, Y. Wang, *et al.*, *ACS Nano*, 2021, **15**, 10775–10981.
- 2 M. Lu, Y. Zhang, S. Wang, J. Guo, W. W. Yu and A. L. Rogach, *Adv. Funct. Mater.*, 2019, 1902008.
- 3 L. N. Quan, B. P. Rand, R. H. Friend, S. G. Mhaisalkar, T. W. Lee and E. H. Sargent, *Chem. Rev.*, 2019, **119**, 7444–7477.
- 4 Q. Wei, M. Li, Z. Zhang, J. Guo, G. Xing, T. C. Sum and W. Huang, *Nano Energy*, 2018, **51**, 704–710.
- 5 M. Lyu, J.-H. Yun, P. Chen, M. Hao and L. Wang, *Adv. Energy Mater.*, 2017, **7**, 1602512.
- 6 S. Wang, J. Popović, S. Burazer, A. Portniagin, F. Liu, K. H. Low, Z. Duan, Y. Li, Y. Xiong, Y. Zhu, *et al.*, *Adv. Funct. Mater.*, 2021, 2102182.
- 7 S. Wang, X. Shen, Y. Zhang, X. Zhuang, D. Xue, X. Zhang, J. Wu, J. Zhu, Z. Shi, S. V. Kershaw, *et al.*, *Small*, 2019, **15**, 1901828.
- 8 Y. Liu, A. Nag, L. Manna and Z. Xia, *Angew. Chem., Int. Ed.*, 2021, **60**, 11592–11603.
- 9 B. M. Benin, D. N. Dirin, V. Morad, M. Worle, S. Yakunin, G. Raino, O. Nazarenko, M. Fischer, I. Infante and M. V. Kovalenko, *Angew. Chem., Int. Ed.*, 2018, **57**, 11329–11333.
- 10 B. Yang, F. Hong, J. Chen, Y. Tang, L. Yang, Y. Sang, X. Xia, J. Guo, H. He, S. Yang, *et al.*, *Angew. Chem., Int. Ed.*, 2019, **58**, 2278–2283.
- 11 G. Volonakis, A. A. Haghighirad, R. L. Milot, W. H. Sio, M. R. Filip, B. Wenger, M. B. Johnston, L. M. Herz, H. J. Snaith and F. Giustino, *J. Phys. Chem. Lett.*, 2017, **8**, 772–778.
- 12 J. Luo, X. Wang, S. Li, J. Liu, Y. Guo, G. Niu, L. Yao, Y. Fu, L. Gao, Q. Dong, *et al.*, *Nature*, 2018, **563**, 541–545.
- 13 F. Locardi, M. Cirignano, D. Baranov, Z. Dang, M. Prato, F. Drago, M. Ferretti, V. Pinchetti, M. Fanciulli, S. Brovelli, *et al.*, *J. Am. Chem. Soc.*, 2018, **140**, 12989–12995.
- 14 J. C. Dahl, W. T. Osowiecki, Y. Cai, J. K. Swabeck, Y. Bekenstein, M. Asta, E. M. Chan and A. P. Alivisatos, *Chem. Mater.*, 2019, **31**, 3134–3143.
- 15 H. Arfin, J. Kaur, T. Sheikh, S. Chakraborty and A. Nag, *Angew. Chem., Int. Ed.*, 2020, **59**, 11307–11311.
- 16 D. Manna, T. K. Das and A. Yella, *Chem. Mater.*, 2019, **31**, 10063–10070.
- 17 Y. Liu, Y. Jing, J. Zhao, Q. Liu and Z. Xia, *Chem. Mater.*, 2019, **31**, 3333–3339.
- 18 S. Jin, R. Li, H. Huang, N. Jiang, J. Lin, S. Wang, Y. Zheng, X. Chen and D. Chen, *Light: Sci. Appl.*, 2022, **11**, 52.
- 19 Y. Liu, X. Rong, M. Li, M. S. Molokeev, J. Zhao and Z. Xia, *Angew. Chem., Int. Ed.*, 2020, **59**, 11634–11640.
- 20 C.-Y. Wang, P. Liang, R.-J. Xie, Y. Yao, P. Liu, Y. Yang, J. Hu, L. Shao, X. W. Sun, F. Kang, *et al.*, *Chem. Mater.*, 2020, **32**, 7814–7821.
- 21 L. Kong, X. Zhang, Y. Li, H. Wang, Y. Jiang, S. Wang, M. You, C. Zhang, T. Zhang, S. V. Kershaw, *et al.*, *Nat. Commun.*, 2021, **12**, 1246.
- 22 W. Yang, P. Dang, G. Zhang, H. Lian, G. Li and J. Lin, *Inorg. Chem.*, 2022, **61**, 5903–5911.
- 23 S. Das Adhikari, C. Echeverria-Arrondo, R. S. Sanchez, V. S. Chirvony, J. P. Martinez-Pastor, S. Agouram, V. Munoz-Sanjose and I. Mora-Sero, *Nanoscale*, 2022, **14**, 1468–1479.
- 24 S. Li, J. Luo, J. Liu and J. Tang, *J. Phys. Chem. Lett.*, 2019, **10**, 1999–2007.
- 25 X. Wang, W. Meng, W. Liao, J. Wang, R. G. Xiong and Y. Yan, *J. Phys. Chem. Lett.*, 2019, **10**, 501–506.
- 26 J. R. Lakowicz, *Principles of Fluorescence Spectroscopy*, Springer, Boston, MA, USA, 3rd edn, 2006.
- 27 S. Wang, Y. Wang, Y. Zhang, X. Zhang, X. Shen, X. Zhuang, P. Lu, W. W. Yu, S. V. Kershaw and A. L. Rogach, *J. Phys. Chem. Lett.*, 2019, **10**, 90–96.
- 28 S. Wang, S. V. Kershaw and A. L. Rogach, *Chem. Mater.*, 2021, **33**, 5413–5421.
- 29 H. Siddique, Z. L. Xu, X. D. Li, S. Saeed, W. T. Liang, X. Q. Wang, C. Gao, R. C. Dai, Z. P. Wang and Z. M. Zhang, *J. Phys. Chem. Lett.*, 2020, **11**, 9572–9578.
- 30 G. Kresse and J. Furthmüller, *Phys. Rev. B: Condens. Matter Mater. Phys.*, 1996, **54**, 11169–11186.
- 31 J. P. Perdew, K. Burke and M. Ernzerhof, *Phys. Rev. Lett.*, 1996, **77**, 3865–3868.
- 32 P. E. Blochl, *Phys. Rev. B: Condens. Matter Mater. Phys.*, 1994, **50**, 17953–17979.
- 33 H. J. Monkhorst and J. D. Pack, *Phys. Rev. B: Solid State*, 1976, **13**, 5188–5192.
- 34 S. Grimme, J. Antony, S. Ehrlich and H. Krieg, *J. Chem. Phys.*, 2010, **132**, 154104–154124.
- 35 S. Grimme, S. Ehrlich and L. Goerigk, *J. Comput. Chem.*, 2011, **32**, 1456–1465.
- 36 S. H. Wei and S. B. Zhang, *Phys. Rev. B: Condens. Matter Mater. Phys.*, 2002, **66**, 155211.
- 37 J. Kang and L. W. Wang, *J. Phys. Chem. Lett.*, 2017, **8**, 489–493.
- 38 I. Levine, O. G. Vera, M. Kulbak, D.-R. Ceratti, C. Rehermann, J. A. Márquez, S. Levchenko, T. Unold, G. Hodes, I. Balberg, *et al.*, *ACS Energy Lett.*, 2019, 1150–1157.
- 39 S. Levy, S. Khalfin, N. G. Pavlopoulos, Y. Kauffmann, G. Atiya, S. Shaek, S. Dror, R. Shechter and Y. Bekenstein, *Chem. Mater.*, 2021, **33**, 2370–2377.
- 40 D. Manna, J. Kangsabanik, T. K. Das, D. Das, A. Alam and A. Yella, *J. Phys. Chem. Lett.*, 2020, **11**, 2113–2120.
- 41 K. Arshak and O. Korostynska, *Microelectron. Int.*, 2002, **19**, 30–34.
- 42 G. Schön, J. Tummavuori, B. Lindström, C. R. Enzell, C. R. Enzell and C.-G. Swahn, *Acta Chem. Scand.*, 1973, **27**, 2623–2633.

- 43 H. Grönbeck, S. Klacar, N. M. Martin, A. Hellman, E. Lundgren and J. N. Andersen, *Phys. Rev. B: Condens. Matter Mater. Phys*, 2012, **85**, 115445.
- 44 Y. Wu, X. Li and H. Zeng, *Small Struct.*, 2020, **2**, 2000071.
- 45 Q. Hu, G. Niu, Z. Zheng, S. Li, Y. Zhang, H. Song, T. Zhai and J. Tang, *Small*, 2019, **15**, e1903496.